01 May 2015

Pore Pressure Evolution and Fluid Flow During Visco-Elastic Single-Layer Buckle Folding

Andreas Eckert
Missouri University of Science and Technology, eckertan@mst.edu

X. Liu

P. Connolly

Recommended Citation

A. Eckert et al., "Pore Pressure Evolution and Fluid Flow During Visco-Elastic Single-Layer Buckle Folding," *Geofluids*, vol. 16, no. 2, pp. 231-248, John Wiley & Sons, May 2015.
The definitive version is available at https://doi.org/10.1111/gfl.12145

GEOFLUIDS

Geofluids (2016) **16**, 231–248 doi: 10.1111/gfl.12145

Pore pressure evolution and fluid flow during visco-elastic single-layer buckle folding

A. ECKERT[1], X. LIU[1] AND P. CONNOLLY[2]

[1]*Department of Geosciences and Geological and Petroleum Engineering, Missouri University of Science and Technology, Rolla, MO, USA;* [2]*Chevron ETC, Houston, TX, USA*

ABSTRACT

Pore pressure and fluid flow during the deformational history of geologic structures are directly influenced by tectonic deformation events. In this contribution, 2D plane strain finite element analysis is used to study the influence of different permeability distributions on the pore pressure field and associated flow regimes during the evolution of visco-elastic single-layer buckle folds. The buckling-induced fluid flow regimes indicate that flow directions and, to a lesser degree, their magnitudes vary significantly throughout the deformation and as a function of the stratigraphic permeability distribution. The modelling results suggest that the volumetric strain and the permeability distribution significantly affect the resulting flow regime at different stages of fold development. For homogeneous permeability models ($k > 10^{-21}$ m^2), low strain results in a mostly pervasive fluid flow regime and is in agreement with previous studies. For larger strain conditions, fluid focusing occurs in the buckling layer towards the top of the fold hinge. For low permeabilities ($<10^{-21}$ m^2), local focused flow regimes inside the buckling layer emerge throughout the deformation history. For models featuring a low-permeability layer embedded in a high-permeability matrix or sandwiched between high-permeability layers, focused flow regimes inside the folded layer result throughout the deformation history, but with significant differences in the flow vectors of the surrounding layers. Fluid flow vectors induced by the fold can result in different, even reversed, directions depending on the amount of strain. In summary, fluid flow regimes during single-layer buckling can change from pervasive to focused and fluid flow vectors can be opposite at different strain levels, that is the flow vectors change significantly through time. Thus, a complete understanding of fluid flow regimes associated with single-layer buckle folds requires consideration of the complete deformation history of the fold.

Key words: buckle folds, fluid flow, permeability, pore pressure, volumetric strain

Received 19 December 2014; accepted 23 April 2015

Corresponding author: Andreas Eckert, Department of Geosciences and Geological and Petroleum Engineering, Missouri University of Science and Technology, 129 McNutt Hall, 1400 N. Bishop Av, Rolla, MO 65409-0410, USA.
Email: eckertan@mst.edu. Tel: +1 573 341 4876; Fax: +1 573 341 6935.

Geofluids (2016) **16**, 231–248

INTRODUCTION

Buckle folds of sedimentary and metamorphic rocks are important examples of hydrocarbon accumulation systems (e.g. Smith-Rouch 2006) and hydrothermal mineral deposits (Ord *et al.* 2002; Yang 2006). The accumulation of fluids and minerals in such systems is dependent on the fluid flow during the deformational history of the geologic structure (Ord & Oliver 1997; Ju *et al.* 2009; Evans & Fischer 2012). It is generally understood that there are a large variety of factors controlling fluid flow in rock masses such as (i) the spatial distribution and evolution of permeability and porosity (e.g. Du Rouchet 1981; Walder & Nur 1984); (ii) plastic deformation leading to enhanced structural permeability (e.g. Sibson 1996; Zhang *et al.* 2007); (iii) variations in the hydraulic head (Hubbert 1953) due to (a) variations in topography (e.g. Bethke & Marshak 1990; Garven 1995), (b) fluid generation in maturing hydrocarbon-bearing sediments (Hubbert & Rubey 1959); and (iv) abnormal pore pressures above hydrostatic level due to tectonic deformation (Oliver 1986; Ge & Garven 1992; Zhang *et al.* 2007, 2011; Cui *et al.* 2012).

To understand the pore pressure evolution and fluid flow associated with buckling, point 4 above becomes of interest. Understanding of the strain distribution in folds and the localization of deformation is important

because it affects fluid mobility (Evans & Fischer 2012). Hydromechanically, tectonic deformation results in pore volume and associated pore pressure changes whereby fluids will flow along hydrologic gradients from regions of elevated pore pressure to regions of decreased pore pressure (e.g. Ge & Garven 1992; Upton 1998; Nemcok *et al.* 2005). Assuming fluid migration follows Darcy's law (Jaeger *et al.* 2007), pore pressure, hydraulic head and permeability determine the fluid velocities. Whilst there exists a vast amount of knowledge in the literature on buckle fold development (e.g. Biot 1961; Ramberg 1963) and the influence of various material parameters such as lithology, rheology, and strain rate (e.g. Hudleston & Treagus 2010 and references therein) on fold amplitude, shape, strain history and the state of total stress, the development of pore pressure or overpressure has often been reduced to the analysis of the mean stress (e.g. Stephansson 1974; Schmalholz *et al.* 2001; Mancktelow 2008). Numerical modelling approaches which couple deformation and fluid flow have become a standard tool for studying pore pressure evolution and deformation driven fluid flow (e.g. Upton 1998; Minkoff *et al.* 2003; McLellan *et al.* 2004; Yang 2006; Zhang *et al.* 2007, 2011). However, the evolution of pore pressure and associated fluid flow pathways during the deformation history of buckle folds has only been studied by Ord & Oliver (1997), and by Zhang *et al.* (2007) for elasto-plastic rheologies.

Ord & Oliver (1997) demonstrate for a single-layer buckle fold that rheology and permeability contrasts are significant factors controlling the flow regime during deformational events. They conclude that pervasive flow is favoured by low permeability and low rheological contrasts under low strain conditions. Focused flow linked to localized deformation is favoured by large permeability and large rheological contrast under large strain conditions. For the single-layer buckle fold considered in their models, fluids are focused towards the fold hinge below the lower permeability layer. For a multilayer fold system, Zhang *et al.* (2007) show that permeability contrasts between layers enable isolated flow patterns to emerge and flow is mostly bedding parallel with fluid focusing during folding occurring towards the fold hinge along high-permeability layers. Fluid flow across low-permeability layers is only observed for fold hinge regions undergoing tensile failure and associated permeability increases.

These studies show that the fluid flow system during deformational events such as buckling is dependent on the material property distribution, mainly the permeability, and the localization of deformation, which in turn may result in plastic strain and hence permeability changes. With respect to fluid accumulation in buckle folds and to assess the conditions of their economic extraction, knowledge of how pore pressure and flow paths evolve during the deformational history of buckle folds is necessary (Evans & Fischer 2012). As presented by Eckert *et al.* (2014), single-layer buckle folding for low-permeability rocks results in significant deformation-related overpressure. Eckert *et al.* (2014) study the effective stress evolution and associated tensile fracture initiation, but do not analyse the resulting fluid flow regimes. To the authors' knowledge, no study comprehensively provides a general understanding of how pore pressure and fluid flow evolve during buckling (from initiation to final buckle shape) for different scenarios of permeability distribution and strain conditions. The recent review paper by Evans & Fischer (2012) presents several conceptual models for fluid systems in fold structures with different structural and stratigraphic configurations, which need to be verified by field studies and numerical analysis. Evans & Fischer (2012) also state that to improve the knowledge of large-scale fold-related fluid systems, a better documentation of fold-related deformation patterns requires high-resolution mechanical-based numerical models accounting for fluid flow and fluid mobility.

This study uses high-resolution 2D plane strain finite element analysis (FEA) to simulate visco-elastic single-layer buckle fold development of one class of rocks under realistic *in situ* stress and pore pressure conditions. The influence of material permeability for different single-layer buckle fold scenarios is studied to gain insight into pore pressure evolution and associated flow pathways both in the folded layer and surrounding matrix during the various stages of the buckling process. The understanding of the resulting fluid flow regime bears important implications for processes such as mineral deposition, hydrocarbon migration, CO_2 storage and groundwater flow. Of particular interest are the spatial and temporal distributions of focused fluid passageways and the locations towards which fluids migrate.

NUMERICAL MODELLING APPROACH

Methodology

In this study, visco-elastic single-layer fold systems are simulated and, following the studies of Mancktelow (1999), Zhang *et al.* (2000) and Schmalholz *et al.* (2001), a classic Maxwell model is adopted. The Maxwell rheology enables instantaneous elastic behaviour for high strain rates and time-dependent viscous behaviour for low strain rates.

For this study, it is assumed that folds extend infinitely along the fold axis and that the displacements of all points in the model are parallel to the *x*-*z* plane. Therefore, a two-dimensional plane strain approach is employed. In addition to the visco-elastic Maxwell rheology, pore pressure is introduced by utilizing effective stress analysis assuming an incompressible fluid and rock matrix, that is utilizing a Biot coefficient of $\alpha = 1$ (Jaeger *et al.* 2007).

Fluid flow is simulated by Darcy's law (Jaeger *et al.* 2007) and is also coupled to the mechanical deformation. The resulting governing diffusion equation for the pore pressure, P_P, is given by:

$$\frac{Kk_x}{\mu_f}\frac{\partial^2 P_p}{\partial x^2}+\frac{Kk_z}{\mu_f}\frac{\partial^2 P_p}{\partial z^2}-\frac{\partial P_p}{\partial t}+\dot{\sigma}^{iso}=0, \quad (1)$$

where $k_{x,z}$ represents the permeability components, μ_f the fluid (i.e. water) viscosity and K the bulk modulus. As can be seen from Eq. 1, pore pressure changes due to mechanical deformation are coupled to the isotropic part of the stress rate tensor and are thus the result of strain-related pore volume changes, whereby pore pressure is increased in regions of contractional strain (i.e. reduction in volume) and pore pressure is decreased in regions of extensional strain (i.e. increase in volume). The detailed derivation of the governing equation system is presented by Eckert *et al.* (2014; i.e. supporting information) and not repeated here.

The finite element method (via the commercial software package ABAQUS™; Abaqus 2014) is employed to solve the equations of equilibrium, conservation of mass, constitutive equations and the equations for pore fluid flow.

Model set-up

Dominant wavelength

To study the pore pressure distribution of buckle folds, the numerical models are setup such that only one wavelength is amplified. Based on the classic single-layer fold theory (e.g. Biot 1961), it has been found that folds are characterized by a dominant wavelength λ_{dv}, which is dependent on the viscosity contrast, R_μ, between the competent (to be folded) layer and the surrounding matrix ($\frac{\lambda_{dv}}{h}=2\pi\sqrt[3]{\frac{\mu_f}{6\mu_m}}$, where h is the layer thickness). To determine an appropriate dominant wavelength for the various models, the approach by Schmalholz & Podladchikov (1999) and Schmalholz *et al.* (2001) is followed using the parameter R which determines whether the competent layer is folded viscously ($R < 1$) or elastically ($R > 1$). R is defined as the ratio between the viscous dominant wavelength, λ_{dv}, and the elastic dominant wavelength,λ_{de}:

$$R=\frac{\lambda_{dv}}{\lambda_{de}}=\sqrt[3]{\frac{\mu_f}{6\mu_m}}\sqrt{\frac{P_0}{G}} \quad (2)$$

where G is the shear modulus, and P_0 is the initial layer parallel stress. For the viscosity μ_f (i.e. 10^{21} Pa s) in the numerical models, the initial layer parallel stress is set such that viscous behaviour dominates and is given by $P_0=4\mu_f\dot{\varepsilon}$ (Schmalholz & Podladchikov 1999). Based on the values used, the parameter R equals 0.12, verifying that deformation is dominated by viscous behaviour. From the analysis above, λ_{dv}/h of 12.74 m is chosen for these models.

Model geometry

The geometry of the 2D finite element model comprises a central single folding layer 30 m thick embedded in a matrix 2 km thick (Fig. 1). The folding layer is characterized by small, periodic, 2.5 m amplitude perturbations of the viscous dominant wavelength. The layer is horizontally compressed using a strain rate of 10^{-14} s^{-1}, representative of a reasonable geologic deformation rate (Twiss & Moores 2007). The overall horizontal model dimension is 1720 m, enabling several fold trains to develop. The folding layer and matrix are distinguished by a stiffness and viscosity contrast R_μ (Table 1). As significant overburden loads are investigated in this study, initial porosity changes with depth are applied after Medina *et al.* (2011):

$$\varphi(z)=16.39e^{-0.00039z}, \quad (3)$$

where φ is the porosity, and z is the depth in metres (relative to the top of the matrix).

Furthermore, as permeability is also a function of depth, the relationship given by Medina *et al.* (2011) is modified to account for lower permeabilities:

$$k(z)=7.583\times10^{-17}e^{0.283\phi}, \quad (4)$$

where ϕ is the porosity, z is the depth in m, and k is the permeability in m^2.

The initial pore pressure distribution in the model is assumed to be hydrostatic, and the permeability is considered to be anisotropic with the horizontal permeability being five times the vertical permeability. The material is defined in ABAQUS™ such that material orientations rotate during buckling (a detailed explanation is given in the Appendix). For the single-layer models, a range of different permeability distributions are tested, ranging from homogeneous high- and low-permeability cases to heterogeneous permeability distributions between the matrix and the folded layer. The different models are listed in Table 1. In Model 5, the folded layer is sandwiched between two layers of high permeability (Fig. 1C)

Initial conditions and boundary conditions

A range of single-layer folding scenarios are investigated. All models utilize several fixed input parameters and boundary conditions (i.e. strain rate, viscosity, viscosity contrast) which are given in Table 2. Although it is clear that each of these parameters has its own influence on the stress and strain distribution during the buckling process, it should be noted that the goal of this study was to investigate the influence of the permeability distribution on the flow vectors and pore pressure evolution during the buckling process. Parameters given by Table 2 represent typical

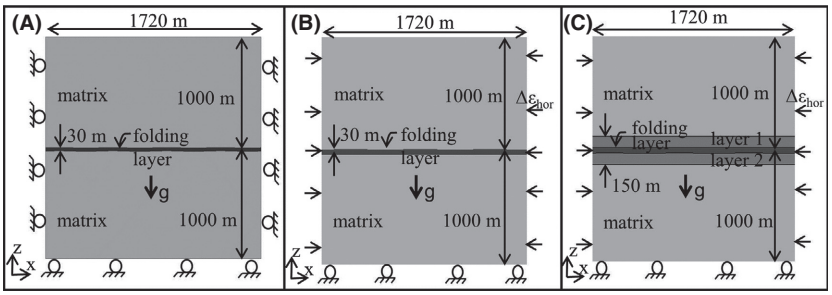

Fig. 1. Model geometry. (A) Boundary conditions for the prestressing load step to reach gravitational equilibrium. (B) In the second load step, horizontal shortening is applied using a strain rate of 10^{-14} s^{-1}. (C) Specific model configuration for Model 5 featuring a low-permeability fold layer embedded in 2 high-permeability layers.

Table 1 Horizontal permeability distributions for the various models.

Model	Permeability fold	Permeability matrix	Permeability Layer 1 and 2
1 a–e	10^{-13} to 10^{-21} m^2	10^{-13} to 10^{-21} m^2	
2	10^{-23} m^2	10^{-23} m^2	
3	10^{-15} m^2	10^{-23} m^2	
4	10^{-23} m^2	10^{-15} m^2	
5	10^{-23} m^2	10^{-23} m^2	10^{-15} m^2

Table 2 Default values of the material properties used in the modelling series.

Properties	Folding layer	Matrix
Specific Gravity	2.75	2.75
Viscosity (μ)	10^{21} [Pa s]	2×10^{19} [Pa s]
Young's Modulus (E)	33.7 ($1–0.1639e^{-0.00039z}$) [GPa] (30 GPa at 1000 m depth)	3.37 ($1–0.1639e^{-0.00039z}$) [GPa] (3 GPa at 1000 m depth)
Poisson Ratio (ν)	0.25	0.25
Permeability (at 1000 m) (K_x)	1.75×10^{-15} [m^2]	1.75×10^{-15} [m^2]
Strain Rate ($\dot{\varepsilon}$)	10^{-14} [s^{-1}]	10^{-14} [s^{-1}]

parameters used in numerical analyses of visco-elastic folding (Mancktelow 1999; Zhang *et al.* 2000; Frehner 2011).

For the fluid flow boundary conditions, the model is simulated as a semiclosed system where fluid flow does not occur across the lateral model boundaries but allowing the pressure build-up to dissipate vertically (Zhou *et al.* 2008).

To simulate realistic *in situ* stress magnitudes in a 2D or 3D numerical model, a stress initialization procedure (termed prestressing), wherein the modelled stresses as a result of gravitational compaction reach a state of equilibrium, is required. A common procedure to simulate realistic *in situ* stresses involves the following steps (Eckert & Connolly 2007; Smart *et al.* 2009; Eckert & Liu 2014; Eckert *et al.* 2014): (i) gravitational prestressing based on the equations of linear poro-elasticity; (ii) application of horizontal strain to simulate the horizontal compression to initiate buckling. Shortening in the *x*-direction is accomplished by applying a constant velocity to the model boundary resulting in 50% bulk shortening over a period of 1.5854 Ma. Whilst the strain rate for each time increment varies throughout the simulation, the overall strain rate to achieve 50% bulk shortening is $10^{-14}s^{-1}$. As a result, the overburden thickness on top of the folded layer gradually increases. For a better understanding of the pore pressure magnitude contours, the spatial references for each deformation stage are shown in Fig. A1 in the Appendix.

MODEL RESULTS FOR THE FOLDED LAYER

For the result analysis which follows, pore pressures and fluid flow vectors are analysed in the folded layer only. Recall, that fluid flow in the numerical models is the result of a combination of Darcy's law (i.e. influenced by the pore pressure gradient and layer permeability), and pore volume changes resulting from the volumetric strain distribution. Additionally, horizontal permeability is five times higher than the vertical permeability, resulting in enhanced horizontal flow if/when it is induced by the heterogeneous volumetric strain distribution. In addition, contour plots of the fluid volume ratio, which is expelled from the folding layer during shortening, are presented in the Appendix (Fig. A2).

Homogeneous permeability distribution

For the permeability analysis, both matrix and folding layers are characterized by the same permeability. Horizontal permeabilities are varied from 10^{-13} m^2 to 10^{-23} m^2 reflecting the large range for sedimentary rocks (Jaeger *et al.* 2007). For the various numerical models considered, the spatial and temporal pore pressure evolution in combination with the resulting fluid flow vectors and fluid velocities are analysed for the stages of 20, 30, 40 and 50% shortening. As the hinge zone of fold structures represents a likely location of fluid accumulation, and the limb a location for fluid transition, the pore pressure evolution is analysed in detail at these places.

Figure 2A shows the evolution of the pore pressure at the top of the hinge during fold formation. For high

permeabilities (10^{-15} m^2), overpressure does not develop and the pore pressure is close to the theoretical hydrostatic value (green line in Fig. 2A,B). For lower permeabilities (10^{-17} to 10^{-23} m^2), the folding layer becomes over-pressured almost instantaneously after the onset of horizontal compression. In the early stages of fold development (<18% shortening), the lowest permeability causes the highest degree of overpressure. For the later stages (>18% shortening), pore pressures steadily increase; at the limb of the fold, the pore pressure evolution follows the same trend as for the top of the hinge (Fig. 2B).

The pore pressure results for 10^{-21} m^2 and 10^{-23} m^2 show that the dependence on permeability, especially after ~16% shortening, is both nonlinear and nonuniform. The highest pore pressure does not occur for 10^{-23} m^2 but for 10^{-21} m^2. This behaviour can be explained by the spatial pore pressure distribution normalized by the subtraction of the hydrostatic value (Fig. 2C,D). It can be seen that for 10^{-21} m^2, the pore pressure in the folding layer and the matrix is hydraulically connected, resulting in pore pressure magnitudes that correlate to depth (Fig. 2C) with the lowest pore pressure of 38.64 MPa occurs (normalized as 19.72 MPa) at the top hinge of the fold (marked A in Fig. 2C) and the highest pore pressure of 41.03 MPa occurs (normalized as 20.79 MPa) at the bottom of the synform (marked B in Fig. 2C). For 10^{-23} m^2 (Fig. 2D), the pore pressure in the folding layer and the matrix are characterized by a steep gradient and the pore pressure is linked to the strain distribution in the layer. The pore pressure is not depth related, and the maximum pore pressure of 41.23 MPa (normalized as 21.75 MPa) occurs at the limb of the fold (marked C in Fig. 2D). The slightly lower pore pressure at the top of the hinge can be explained by the slightly higher extensional strain developed here.

Permeability range (10^{-13} m^2 to 10^{-21} m^2): Model 1

To illustrate the impact of permeability on flow within the folding system, the 10^{-15} m^2 permeability case is shown in Fig. 3 featuring the fluid velocity vectors and magnitudes in combination with the spatial pore pressure and volumetric strain distribution. Fluid flow velocities across all deformation stages are in the order of 10^{-12} to 10^{-13} ms^{-1} (i.e. 31.536 to 3.536 m Ma^{-1}; Fig. 3A). The fluid flow vectors in the initial stage of shortening (i.e. ~5%; not shown) show vertical upward flow accommodating the hydrostatic pore pressure distribution. Although the pore pressure remains hydrostatic (i.e. the pore pressure gradient is 9.81 MPa km^{-1}) throughout the deformation history (Fig. 3B), a vertical component of fluid flow (i.e. upward flow) is observed for all deformation stages. This can be explained by the dynamic evolution of the pore pressure as the model deforms (i.e. the overburden thickness gradually increases). This dynamic pore pressure evolution results in $\Delta P_p/\Delta t \neq 0$ (Fig. A3; Appendix) throughout the deformation history. Once deformation is stopped, static pore pressure equilibrium is achieved which results in $\Delta P_p/\Delta t = 0$ and zero fluid velocity (Fig. A3; Appendix). It should also be recalled that the initial horizontal permeability in the undeformed model is five times higher than the vertical permeability. The material is defined in ABAQUS™ such that the horizontal

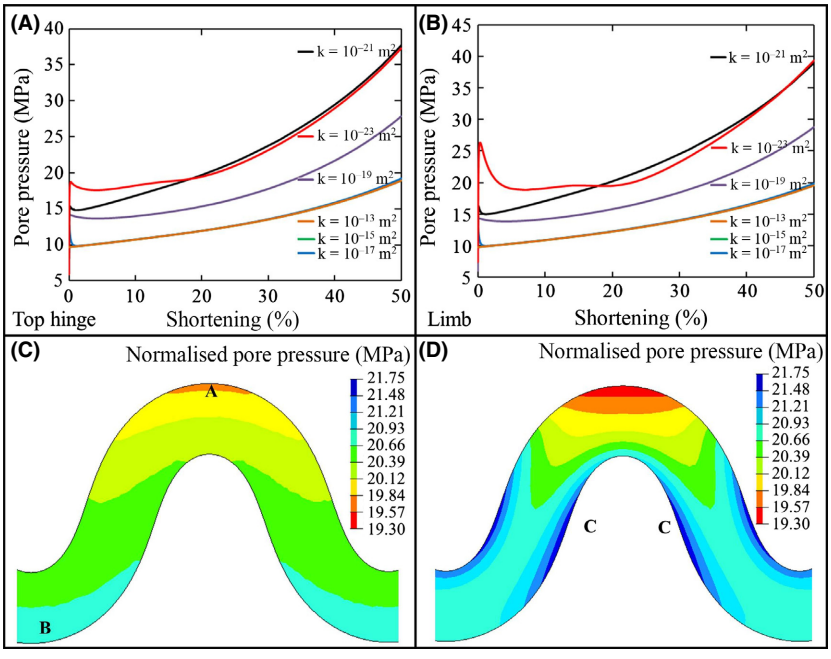

Fig. 2. (A) Pore pressure evolution at the fold hinge. Permeabilities of 10^{-13} to 10^{-17} m^2 do not result in overpressure, and pore pressure is hydrostatic. Lower permeabilities exhibit over-pressure, whereby the highest pore pressure at the hinge is obtained for 10^{-21} m^2. (B) Pore pressure evolution at the fold limb showing the same trend as for the hinge. (C) Normalized pore pressure magnitudes for 10^{-21} m^2 are depth dependent, with maximum and minimum values occurring at the bottom of the synform and top of the antiform. (D) Normalized pore pressure magnitude for 10^{-23} m^2 is linked to the strain distribution, with the maximum pore pressure occurring in the limb.

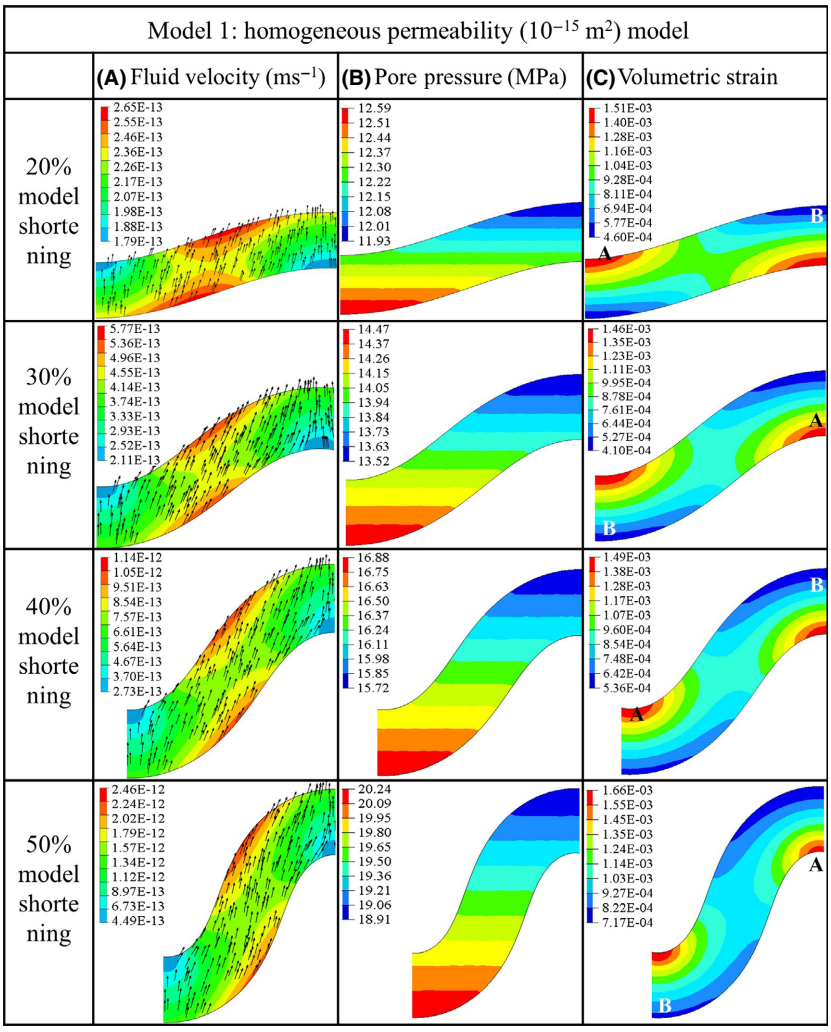

Fig. 3. Results for the models featuring a homogeneous permeability distribution (10^{-13} m^2 to 10^{-21} m^2) for the various deformation stages investigated. (A) Fluid flow vectors (black arrows) and magnitudes (contours). (B) Pore pressure contours. (C) Volumetric strain.

permeability remains layer parallel as the model deforms (Fig. A4; Appendix). As the material orientation changes during the deformational history, layer parallel flow, that is vertical flow in the limb in the late deformation stages, is enhanced.

The fluid flow vectors (Fig. 3A) are hence the result of the combination of the development of hydrostatic pore pressure and the influence of the volumetric strain distribution, that is flowing from regions of high strain (marked A in Fig. 3C) to regions of low strain (marked B in Fig. 3C). As a result, different flow regimes can be observed at different deformation stages. Whilst flow is pervasive for 5, 20 and 30% of shortening, for 40 and 50% shortening a focused flow regime featuring layer parallel flow in the limb and fluid migration towards the top of the hinge zone in the antiform are established.

As illustrated in Fig. 2, permeabilities $\leq 10^{-19}$ m^2 result in overpressure; however, the flow vectors show the same orientations throughout the deformation history as shown in Fig. 3A, although having lower range of magnitudes (10^{-12} to 10^{-13} ms^{-1}, or 31.536 to 3.536 m Ma^{-1} for permeabilities ranging from 10^{-13} m^2 to 10^{-19} m^2, and 10^{-14} to 10^{-15} ms^{-1}, or 31.536 to 3.536 cm Ma^{-1} for 10^{-21} m^2).

Extremely low permeability ($k = 10^{-23}$ m^2): Model 2

For the case with extremely low permeability, the fluid flow vectors show very small magnitudes of 10^{-16} to 10^{-17} ms^{-1} (Fig. 4A). Over the time scale of deformation modelled (i.e. 1.5 million years), a final fluid displacement of only 1.5 cm is observed, indicating almost immobile fluids. During the 20 and 30% deformation stages, fluid flow is occurring towards the centre of the fold layer, originating both from the top and the bottom of the layer (marked A in Fig. 4A). The over-pressured pore pressure distribution does not correlate to depth, and a region of lower pore pressure is present across the centre of the folding layer, attracting fluids. As can be

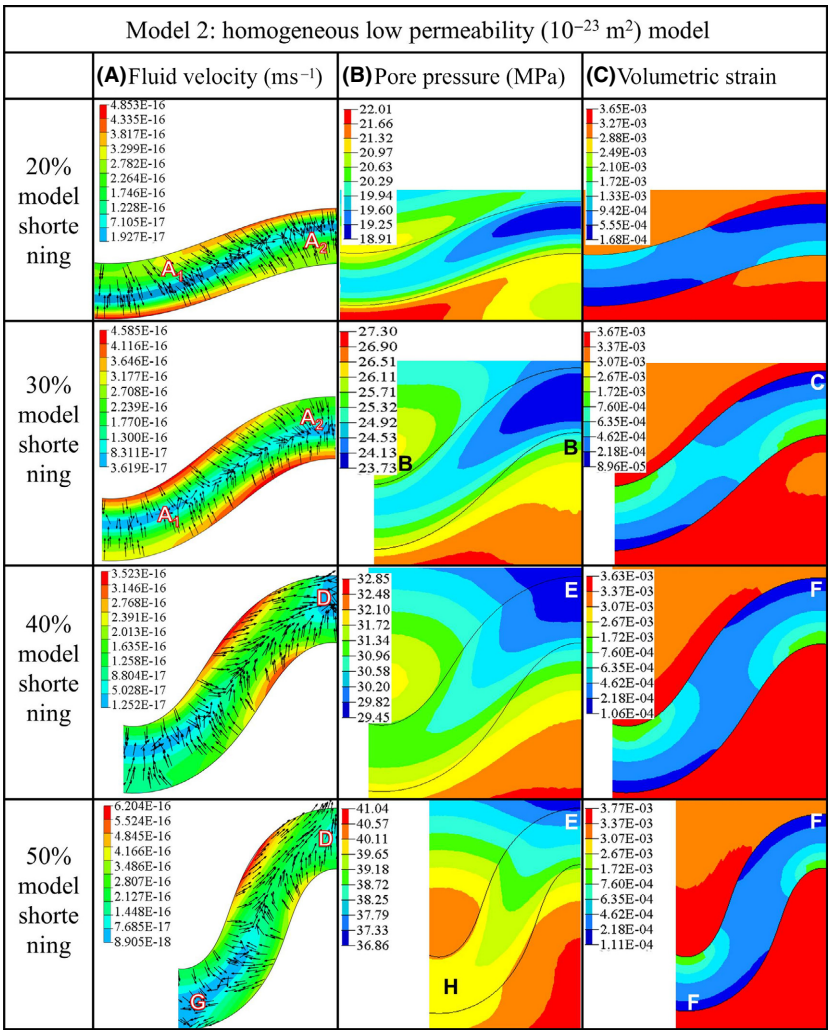

Fig. 4. Results for Model 2 ($k = 10^{-23}$ m^2) for the various deformation stages investigated. (A) Fluid flow vectors (black arrows) and magnitudes (contours). (B) Pore pressure contours. (C) Volumetric strain.

seen for 30% shortening, the highest relative pore pressure magnitudes occur in the matrix directly above the synform and below the antiform (marked B in Fig. 4B). As the fold layer is more competent than the matrix (i.e. has a higher bulk modulus), lower contractional strain is localized in the fold (Fig. 4C) and lower pore pressures result. The pore pressure minimum occurring at the top of the hinge zone of the fold can be explained by the lowest contractional strain occurring here (i.e. relative extension; marked C in Fig. 4C). For the stages of 40 and 50% of shortening, the fluid flow vectors for the upper half of the fold train point towards the top of the hinge (marked D in Fig. 4A), showing dependency on the local strain distribution, that is flowing towards the minimum volumetric strain (marked F in Fig. 4C) and hence the minimum pore pressure (marked E in Fig. 4B). For the bottom section of the fold at 50% shortening, fluids migrate towards the bottom of the synform (marked G in Fig. 4A), indicating that the flow induced by the low volumetric strain (marked F in Fig. 4C) overcomes the pore pressure gradient, which is at a maximum here (marked H in Fig. 4B).

Heterogeneous permeability distribution

High-permeability fold, low-permeability matrix: Model 3

Figure 5A shows the fluid flow vectors and magnitudes where it can be seen that the fluid flow velocities (~10^{-15} ms^{-1}) comprise essentially a closed system in a low-permeability matrix. The low-permeability matrix results in overpressure throughout the model domain. Due to the high permeability in the folded layer, the pore pressure distribution is depth correlated for all deformation stages (Fig. 5B). However, the fluid flow vectors (Fig. 5A) are not significantly affected by the vertical pore pressure gradient, especially for 20 and 30% shortening. For these two stages, the pore pressure difference, ΔP_P, between the top of the hinge in the antiform and the bottom of the synform is 0.7 MPa and 1 MPa, respectively. This low pore pressure gradient results in flow

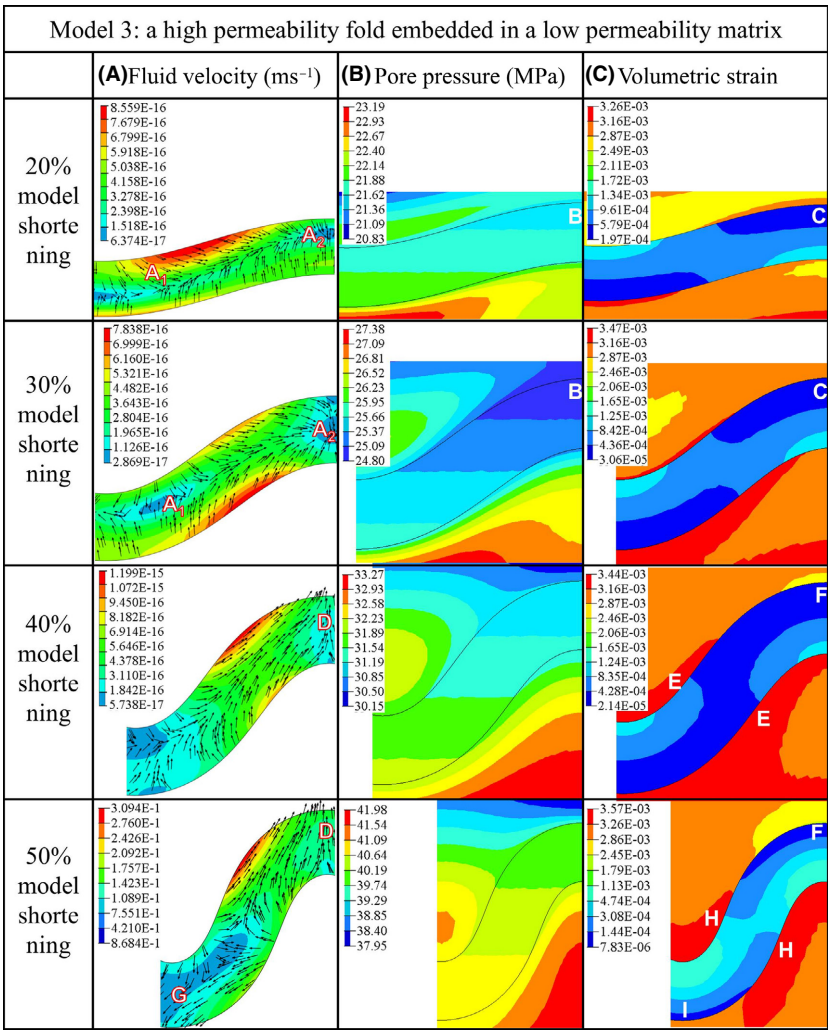

Fig. 5. Results for Model 3 for the various deformation stages investigated. (A) Fluid flow vectors (black arrows) and magnitudes (contours). (B) Pore pressure contours. (C) Volumetric strain.

vectors being influenced by the strain distribution. Similar to the model featuring extremely low permeability, fluids are driven towards the centre of the folded layer (marked A_1 in Fig. 5A) and towards the top of the hinge zone (marked A_2 in Fig. 5A), where the lowest pore pressure occurs (marked B in Fig. 5B), and which also features the lowest volumetric strain values (marked C in Fig. 5C). For the later deformation stages (40 and 50%), the increased amount of strain has a larger influence on the fluid flow vectors, resulting in a more focused flow regime. In the upper half of the fold, fluids flow from regions of higher contractional volumetric strain in the matrix surrounding the folded layer (marked E in Fig. 5C) towards the top of the hinge (Fig. 5A), where the lowest volumetric strain occurs (marked F in Fig. 5C). The reverse pattern of fluid flow can be observed towards the bottom of the synform; fluids flow towards the bottom of the synform (marked G in Fig. 5A) and are driven by the higher contractional volumetric strain in the matrix surrounding the folded layer (marked H in Fig. 5C), as well as the low volumetric strain at the bottom of the synform (marked I in Fig. 5C).

Low-permeability fold, high-permeability matrix: Model 4

The fluid flow vectors for this model show a uniform and equal response across all deformation stages. Fluids are driven layer perpendicular towards the overburden (Fig. 6A). This can be explained by the large pore pressure difference (14.61 MPa for 20%, 19.33 MPa for 30%, 24.28 MPa for 40%, and 32.40 MPa for 50%) between the upper, high-permeability matrix and the lower part (marked A and B in Fig. 6B). Due to this large pore pressure gradient, fluids in the folded layer hence flow perpendicular to the contours of equal pore pressure.

MODEL RESULTS IN MATRIX LAYERS

The pore pressures and fluid flow vectors are now analysed for the high-permeability matrix below a low-permeability folding layer.

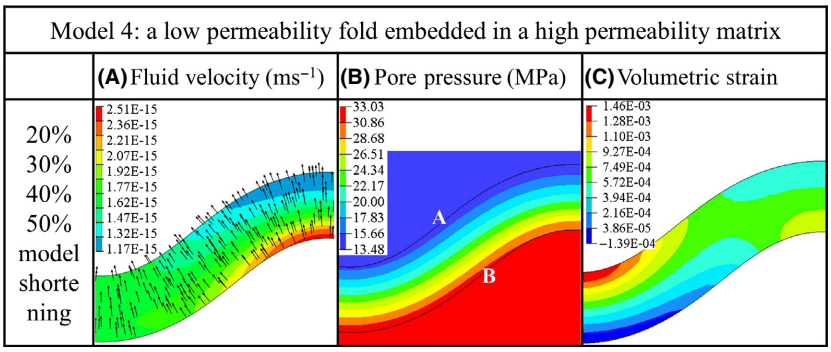

Fig. 6. Results for Model 4 for the various deformation stages investigated. (A) Fluid flow vectors (black arrows) and magnitudes (contours). (B) Pore pressure contours. (C) Volumetric strain.

Low-permeability fold, high-permeability matrix

For the special case of Model 4 (for the matrix below the folded layer), the pore pressure and fluid flow vectors are analysed separately. This case could represent an analogue of a stiff cap rock layer over a permeable host rock of hydrothermal minerals or hydrocarbons. Of particular interest is how the strain induced by the buckled layer, in combination with its characteristic as a permeability barrier, induces or affects the fluid flow regime below it.

Figure 7A,C shows the resulting fluid flow vectors plotted on top of the pore pressure contours for 20 and 50% shortening, respectively. For both deformation stages, fluids are mainly driven upward into the space below the antiform (marked A in Fig. 7A,C), a commonly recognized location for fluid accumulation (Evans & Fischer 2012). It can be seen that pore pressure follows a hydrostatic gradient, which is responsible for the upward flow observed. The fan-like rotation of flow vectors towards the edge of the fold structure is influenced by the volumetric strain distribution which shows a concentrated low below the hinge zone of the fold (marked B in Fig. 7B). For 50% shortening, the upward and outward rotation below the antiform towards the fold limbs (marked C in Fig. 7D) is the result of lower volumetric strain in the fold limbs, below the antiform.

Low-permeability fold variation: Model 5

Model 4 featuring a low-permeability fold layer atop a high-permeability layer merits further consideration as variations of this configuration may resemble fluid flow regimes observed in natural reservoir–caprock sequences. In order to consider this case, the model configuration is modified to include a low-permeability fold layer sandwiched between two layers of high permeability, which are in turn embedded in a low-permeability matrix (Model 5; Fig. 1C). The material properties for the 5 models are given in Table 2. Figure 7A–H shows a comparison between models 4 and 5, displaying the resulting fluid flow vectors plotted on top of the pore pressure contours and the volumetric strain distribution for 20 and 50% shortening, respectively. For both deformation stages, the pore pressure gradient in the layers above and below the matrix is hydrostatic, albeit featuring over-pressured magnitudes due to the low-permeability overburden.

For 20% shortening, the fluid flow vectors below the folded layer are pointing upwards, indicating that the vertical pore pressure gradient is the main fluid driver (marked D in Fig. 7E). In addition, the volumetric strain distribution here indicates lower contractional strain below the antiform (marked E in Fig. 7E), thus assisting in the upward flow. In the low-permeability layer above the folded layer, fluids are focused downwards, towards the top of the hinge zone of the folded layer (marked F in Fig. 7F). This is in contrast to the vertical pore pressure gradient, and contrasts with the results from Model 4, where fluids follow the pore pressure gradient (Fig. 7A). Whilst the volumetric strain for Model 4 (Fig. 7B) only shows minor influence on the fluid flow directions, the downward flow towards the top of the hinge of the fold can be explained by the low volumetric strain in the folded layer (marked G in Fig. 7F), thus attracting fluids.

For 50% shortening, the fluid flow vectors below the folded layer are pointing downwards (marked H in Fig. 7G), the opposite direction from what is shown in Model 4 (Fig. 7C). Although featuring the same permeability in the layer below the fold, the opposing fluid directions for 50% shortening can be explained by the volumetric strain distribution. For Model 4, the volumetric strain below the antiform is on the order of 10^{-4} (Fig. 7D). Due to these small magnitudes, it is obvious that the strain distribution does not significantly affect the fluid vectors, otherwise some downward flow would occur from the area of contractional strain below the antiform (marked I in Fig. 7D) to the area of extensional strain below the synform (marked J in Fig. 7D). For Model 5, contractional strain magnitudes are much larger (10^{-3}) and the strain contours show the transition from higher contractional strain just below the antiform (marked K in Fig. 7D) to lower contractional strain at greater depths

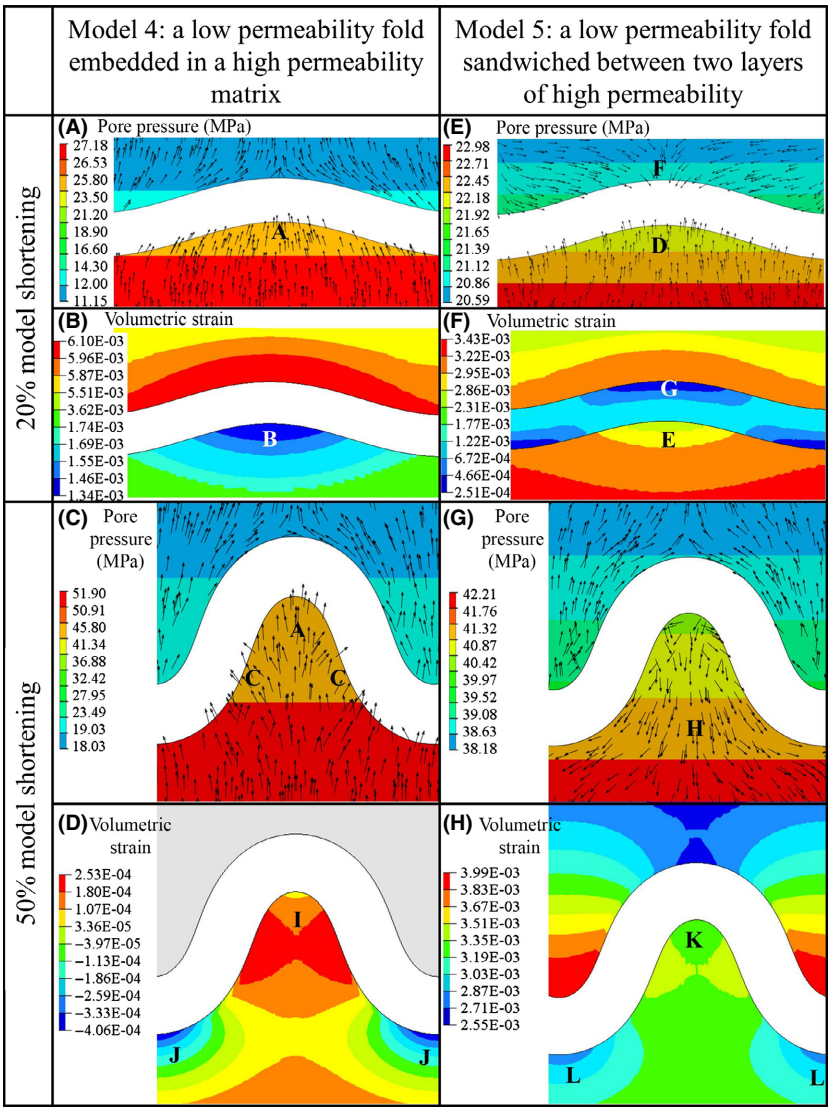

Fig. 7. (A) Fluid flow vectors and pore pressure contours for Model 4 for 20% shortening. (B) Volumetric strain distribution for Model 4 for 20% shortening. (C) Fluid flow vectors and pore pressure contours for Model 4 for 50% shortening. (D) Volumetric strain distribution for Model 4 for 50% shortening. (E) Fluid flow vectors and pore pressure contours for Model 5 for 20% shortening. (F) Volumetric strain distribution for Model 5 for 20% shortening. (G) Fluid flow vectors and pore pressure contours for Model 5 for 50% shortening. (H) Volumetric strain distribution for Model 5 for 50% shortening.

(marked L in Fig. 7H). This indicates that the fluid flow contribution induced by the volumetric strain is overcoming the vertical pore pressure gradient, resulting in downward flow vectors.

The difference in volumetric strain magnitudes at 50% shortening between Model 4 and 5 represents an interesting situation. Model 5 has contractional strain throughout all deformation stages, whereas extensional strain is developed in Model 4. This behaviour can be explained by considering the pore pressure magnitudes for the two models throughout the deformation history. Figure 8 shows that both model configurations result in overpressure. In Model 4, the folded layer is the main permeability barrier and results in a large pore pressure difference (ΔP_P = ~32.40 MPa) between the hydrostatic overburden and the layer below the fold. The resulting pore pressure gradient of 790.15 MPa km^{-1} in the folded layer (marked A and B in Fig. 8A,C) yields a pore pressure of ~51 MPa below the folded layer (below B in Fig. 8A,C). In comparison, the low-permeability overburden is controlling the degree of overpressure for Model 5, albeit at a lower magnitude of 42.99 MPa km^{-1} (marked C in Fig. 8B), resulting in P_P = 37.64 MPa on top of the high-permeability layer. The subsequent increase in pore pressure in the high-permeability layer follows the hydrostatic gradient (marked D in Fig. 8B) and is only slightly increased in the low-permeability fold layer, following a pore pressure gradient of 51.8 MPa km^{-1} (marked E in Fig. 8B). This results in a pore pressure of ~40 MPa below the folded layer (marked F in Fig. 8D), a much smaller magnitude of overpressure compared to Model 4. The higher pore pressure magnitudes in Model 4 result in lower effective stresses and hence explain the lower strain magnitudes.

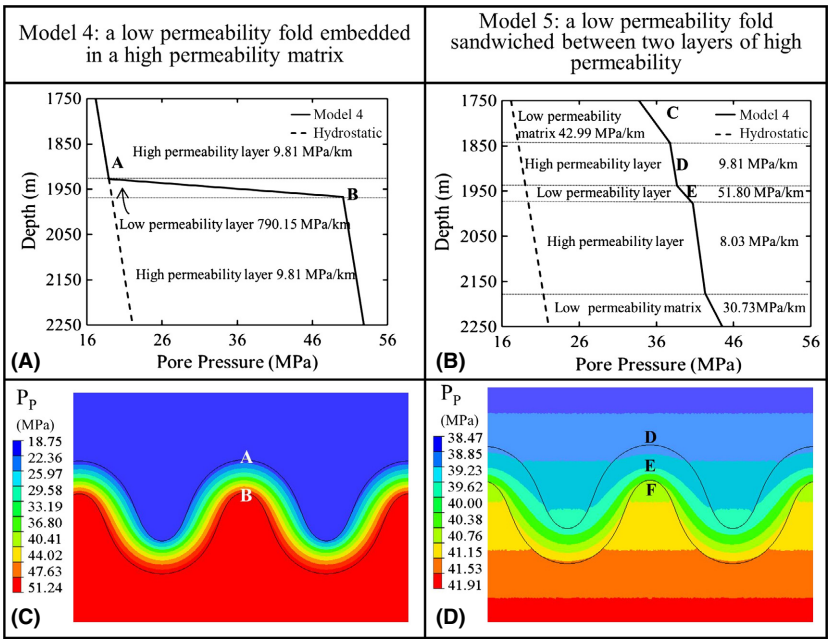

Fig. 8. Pore pressure depth profile (A,B) and pore pressure contours (C,D) and for Models 4 and Model 5. The permeability distribution in Model 4 causes a much larger pore pressure gradient in the folded layer compared to Model 5, resulting in the differences in the strain distribution as observed in Figure 7.

SUMMARY AND DISCUSSION

Numerical modelling results show that the mechanical material properties and their competence contrast are mainly responsible for the strain distribution in buckle fold structures (e.g. Frehner 2011). Through the volumetric strain – pore pressure coupling, pore pressure, and hence fluid flow directions are affected such that flow vectors are not just a function of the evolving permeability distribution. As stated by Ord & Oliver (1997), fluid flow based on mean stress or pore pressure alone may be misleading. For single-layer buckle folds, the numerical modelling results presented here show that a distinction has to be made between models featuring homogeneous and heterogeneous permeability distributions.

For the homogenous models, different flow regimes throughout the deformation history can be observed (Figs 3 and 4). During the initial 30% of deformation, a pervasive flow regime dominates. The fold layers and the matrix are hydraulically coupled, and the pore pressure reaches hydrostatic conditions correlated to depth. For permeabilities $\geq 10^{-17}$ m^2, a hydrostatic pore pressure gradient is established. For lower permeabilities ($<10^{-17}$ m^2), depth-correlated overpressure occurs and results in upward flow. The slight deviation is an early indicator of the strain influence on the fluid flow paths. For deformation stages from 40 to 50% shortening, the influence of the volumetric strain becomes more dominant and the flow vectors become almost layer parallel, indicating a focused flow regime towards the top of the antiform. The results for 20 and 30% of shortening are in agreement with observations from Ord & Oliver (1997) who conclude that pervasive flow is favoured by low-permeability and low rheological contrasts under low strain conditions. The results presented here show that focused flow is also possible when a system with a low-permeability contrast is subject to a higher degree of strain (40 and 50% of shortening).

For a homogeneous model featuring very low permeability (10^{-23} m^2), the strain distribution in the fold layer influences the flow regime, initially focusing fluids towards the centre of the layer, and then later towards the top of the hinge of the antiform. However, due to the very low permeability, fluid velocities are extremely low (i.e. ~10^{-17} ms^{-1}).

For the heterogeneous model featuring a high-permeability fold layer in a low-permeability matrix, a focused flow regime is established throughout the deformation history. For low deformation amplitudes (up to 30% shortening), fluid focusing towards the centre of the fold layer occurs, and at larger amplitudes (30–50%), a splitting of the fluid flow regime is observed: fluids in the upper half of the fold are driven towards the top of the hinge, fluids in the lower half are driven towards the bottom of the synform. These results are in agreement with observations from Ord & Oliver (1997) who state that focused flow linked to localized deformation (i.e. the volumetric strain distribution) is favoured by large permeability and large rheological contrast under large strain conditions. In addition, the results agree with modelling results from Zhang *et al.* (2007) who show that due to the permeability contrasts between layers in a multilayer fold system, isolated flow patterns emerge and flow is mostly bedding parallel, and fluid is focused through high-permeability layers towards the fold hinge. Fluid flow

across low-permeability layers is only observed in fold hinge regions undergoing tensile failure and associated permeability increases. This focused flow regime is also in partial agreement with the conceptual fold – fluid flow model proposed by Evans & Fischer (2012) of a stratified fluid structure and stratabound fluid influx along high-permeability layers. However, the fluid flow pathways proposed by Evans & Fischer (2012), where fluids flow upwards towards the top of the hinge and then downwards, disagree with fluid flow patterns at high deformation stages where fluids on both sides of the fold hinge are driven towards it.

The numerical modelling studies by Ord & Oliver (1997) and Zhang *et al.* (2007) represent a first step in providing a general understanding of the fluid flow – deformation interaction during folding. The model study presented here is in agreement with these studies and provides additional insights to this process as the complete deformation history, and the associated fluid regime is analysed. This study shows that during different deformation stages the combination of permeability contrast and strain distribution is responsible for different fluid flow regimes. In particular, results from models featuring a low-permeability fold layer either embedded in a high-permeability matrix (Model 4), or sandwiched between two layers of high permeability which in turn are embedded in a low-permeability matrix (Model 5), present interesting implications for buckling-induced deformation and the resulting fluid flow pattern in the surrounding rock layers. For Model 4, fluid flow below the fold layer is pervasive for all deformation stages and directed upwards, resulting in a possible fluid accumulation scenario below the antiform structure. For hydrocarbon flow regimes where the vertical flow regime is assisted by the buoyancy effect of lower density hydrocarbons, this confirms the well-known role of anticlines as being premier structural traps. In contrast, for Model 5, the fluid flow regime is different for different deformation stages. Low strain results in upward flow below the antiform and is very similar to Model 4; high strain results in downward flow. This difference is the result of the volumetric strain and pore pressure evolution. As shown in Fig. 8, the evolution of over-pressure is different for both models. The low-permeability fold layer in the high-permeability matrix results in a larger degree of over-pressure, which implies that the pore pressure evolution is dependent on the depth and thickness of the low-permeability layer. To the authors' knowledge, such a relationship is not documented in the literature and requires further analysis (including the depth and thickness of the low-permeability layer, as well as the permeability contrast) to provide a consistent understanding.

It should be noted that the interesting behaviour shown by the heterogeneous permeability distributions is based on the mechanical interactions induced by a single-layer buckle fold (i.e. the mechanical properties for the layers surrounding the fold layer and the matrix are the same). Further studies based on a more realistic multilayer fold system similar to the study by *Zhang et al.* (2007) are necessary to include the mechanical interactions (i.e. the volumetric strain), induced by the multilayer system. Of particular interest in such a system is the influence of rheological contrasts between the different layers. As shown by Frehner (2011), the competence contrast between layers significantly affects the strain distribution of the fold system and is thus expected to have a profound influence on the induced fluid flow.

The resulting fluid flow regime for a homogeneous low-permeability model (fluid flow vectors shown in Fig. 3) could also be applicable to metamorphic systems at greater depth ($z > 20$ km; Ingebritsen & Manning 2010), as the permeability contrast between the fold layer and the matrix would be small in an overall low-permeability environment when depth–porosity–permeability relationships such as Eqs 3 and 4 (Medina *et al.* 2011) are applied. However, it is important to note that simulation of deformation-related pore pressure evolution and fluid flow at greater depth must consider several additional processes including, but not limited to, active thermal dehydration reactions (e.g. Nakajima *et al.* 2009), thermal stress evolution and creep rheology at depth (i.e. dislocation or diffusion creep).

Implications for fractures and fracture-related fluid flow

Investigations of natural fold systems contribute to the understanding derived from numerical studies and serve as an important verification method. One major observation from natural case studies is the influence of natural fracture systems associated with the process of folding. The occurrence of these fracture sets is well documented and understood in the literature (e.g. Price 1966; Ramsay 1967; Price & Cosgrove 1990; Eckert *et al.* 2014). These fractures are hydraulically linking different stratigraphic units and provide fluid pathways across layer boundaries. Further, these fractures are prime location for the mineralization of hydrothermal ore deposits and their occurrence or lack of occurrence helps to evaluate seal efficiency.

It is clear that the modelling approach used does not incorporate failure and associated permeability changes, which represents an integral part of deformation-controlled fluid flow analysis as observed for elasto-plastic models (e.g. Ord & Oliver 1997; Upton 1998; Yang 2006; Zhang *et al.* 2007). It should be noted that in order to study a large deformation range (i.e. 0–50% strain) during buckle folding, a visco-elastic modelling approach is chosen here. Adding plasticity via a Drucker–Prager or similar failure criterion, whilst possible to implement in ABAQUS™, has resulted in severe convergence problems at larger strains, a

problem also observed by Zhang *et al.* (2007), who in their elasto-plastic modelling study could only investigate ~9% of strain. Ideally, visco-elasto-plastic-brittle constitutive models should be used.

To assess the potential of rock failure, the state of stress resulting from the various models is analysed. As a 2D plane strain approach is followed, only the occurrence of tensile fractures parallel to the fold axis at the top of the hinge (Price & Cosgrove 1990), thrust faults at the bottom of the hinge (Price & Cosgrove 1990) and shear fractures in the fold limb can be considered. Figure 9A,B shows the temporal evolution of maximum and minimum effective principal stresses (σ'_1 and σ'_3, respectively) for the fold hinge and the fold limb for the models featuring permeabilities of 10^{-13} m^2 and 10^{-19} m^2. Tensile stresses (i.e. $\sigma'_3 < 0$; Fig. 9A) at both the top of the hinge either do not occur (for $k > 10^{-19}$ m^2) or are <2 MPa (for $k = 10^{-19}$ m^2). For the fold limb, tensile stresses do not occur (Fig. 9B), making tensile failure unlikely for these model scenarios. Shear failure in the limb is also unlikely as the differential stress is too low. For the bottom of the hinge zone, the differential stress is increased (Fig. 9C). For the maximum differential stress obtained at ~18% shortening (as indicated by the solid black line in Fig. 9C; for low-permeability folds), thrust faults are likely to occur for rocks with an assumed cohesive strength of $S_0 \leq$ ~8 MPa, as observed by the Mohr circle plot in Fig. 9D. For the three models with the lowest matrix permeability of 10^{-23} m^2 (i.e. models 2, 3 and 5), Fig. 10A,B shows the temporal evolution of σ'_1 and σ'_3 for the fold hinge and the fold limb. Tensile stress magnitudes of ~6 MPa occur at the top of the hinge and tensile fractures parallel to the fold axis and normal to the bedding are likely to occur. Tensile stresses do not occur in the fold limb (Fig. 10B). Shear failure in the limb is also unlikely as the differential stress is too low. The bottom of the hinge zone exhibits the same behaviour as for the higher permeability models as shown in Fig. 9C,D; thrust faults are likely to occur in this region.

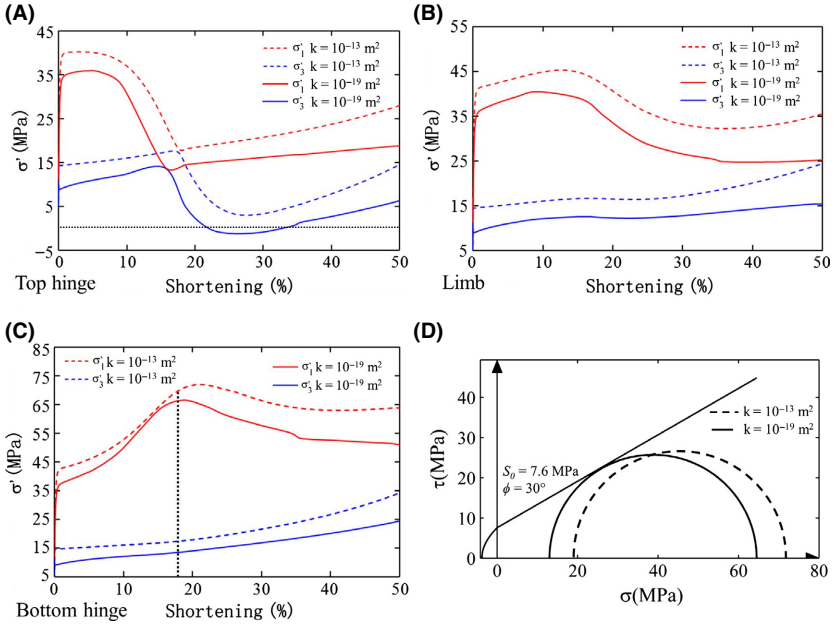

Fig. 9. Maximum and minimum principal stress evolution for the various locations in the fold where failure is commonly observed. (A) At the top of the hinge zone tensile stresses as an indicator to initiate tensile fractures are unlikely or of minor magnitude for model with permeabilities of 10^{-19} m^2 or higher. (B) In the fold limb, tensile stresses are not present and the differential stress is also too low to initiate shear failure. (C) For the bottom of the hinge zone, the maximum differential stress at ~18% indicates shear failure. (D) Mohr circle plots to indicate the likelihood of shear failure for low rock strengths.

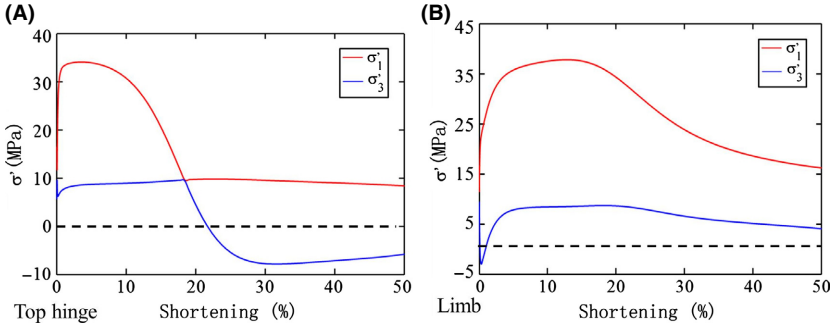

Fig. 10. Maximum and minimum principal stress evolution for the top of the hinge zone and the fold limbs for models featuring a low-permeability fold layer. (A) Tensile stresses are present at the top of the hinge zone, and tensile fractures are likely to occur. (B) For the limb, minor tensile stresses of ~2 MPa are only occurring during the initial 2% of horizontal compression.

These results show that failure is likely only in isolated conditions/locations at the fold hinge, and that widespread failure which occurs across layer boundaries and affects the fluid flow regime is unlikely. The results presented thus do not reproduce the widespread failure observed by Zhang *et al.* (2007). It needs to be repeated here that Zhang *et al.*'s (2007) results are based on an elasto-plastic modelling approach where the instantaneous elastic response tends to result in higher stress magnitudes compared to the visco-elastic approach employed here, during which stresses are constantly relaxed. Furthermore, the stress evolution in an elasto-plastic rheology depends on whether rocks are characterized by strain hardening or strain softening. It is clear that including plastic and brittle failure and their influence on the fluid flow regime would require analysis of the mechanical model property distribution between different layers and is hence best suited for a true multilayer fold system. This represents an extensive sensitivity analysis which is the topic of a separate study and thus is beyond the scope of this contribution.

CONCLUSIONS

The results of single-layer buckling-induced fluid flow models show that fluid flow directions, and to a lesser degree their magnitudes, vary significantly depending on the stratigraphic permeability distribution, and throughout the temporal evolution of deformation. The results of this modelling study suggest that depending on the state of deformation, either the volumetric strain or the permeability distribution affect the fluid flow. This study has shown that understanding fluid flow regimes in single-layer buckle folds and fluid flow regimes induced by single-layer buckle folds requires the study of the complete deformation history as well as the material parameter distributions. Fluid flow regimes can change from pervasive to focused and fluid flow vectors can change significantly through time.

For homogeneous permeability models ($>10^{-21}$ m^2), low strain results in a mostly pervasive fluid flow regime and is in agreement with previous studies. For larger strain conditions, fluid focusing in the fold layer towards the top of the hinge of the fold occurs. This indicates that focused flow is possible for low-permeability contrasts, albeit requiring a higher degree of strain. For low permeabilities ($<10^{-21}$ m^2) focused flow regimes inside the folded layer emerge throughout the deformation history which is consistent with observations from independent studies.

For models featuring a low-permeability layer embedded in a high-permeability matrix (Model 4) or sandwiched between high-permeability layers (Model 5), also focused flow regimes result throughout the deformation history. In these models, however, significant differences arise in the flow vectors in the surrounding layers. Fluid flow vectors induced by the fold in Model 5 result in different (i.e. opposite) directions depending on the amount of strain in the model.

In summary, this study shows that understanding fluid flow regimes in single-layer buckle folds and fluid flow regimes induced by single-layer buckle folds requires consideration of the total deformation history of fold systems. The volumetric strain distribution exerts different levels of influence on the resulting fluid flow regime. In order to improve our understanding of these coupled processes, more studies, preferably extended to multilayer fold systems and more representative constitutive behaviours are necessary to pinpoint whether volumetric strain or permeability significantly affects for fluid flow.

ACKNOWLEDGEMENTS

This work was supported and funded by Chevron ETC. Their permission to publish this work is gratefully acknowledged. We would like to thank Mark Fischer, an anonymous reviewer and the editor Craig Manning for their valuable and constructive reviews, which greatly improved the manuscript. The data for this paper are available at the Department of Geosciences and Geological and Petroleum Engineering at Missouri University of Science and Technology by contacting the corresponding author.

REFERENCES

Abaqus (2014) *ABAQUS Documentation*. Dassault Systèmes, Providence, RI, USA.

Bethke EM, Marshak S (1990) Brine migrations across North America - the plate tectonics of groundwater. *Annual Review of Earth & Planetary Science*, **18**, 287–315.

Biot MA (1961) Theory of folding of stratified viscoelastic media and its implications in tectonics and orogenesis. *Geological Society of America Bulletin*., **72**, 1595–620.

Cui T, Yang J, Samson IM (2012) Tectonic deformation and fluid flow: implications for the formation of unconformity-related uranium deposits. *Economic Geology*, **107**, 147–63.

Du Rouchet J (1981) Stress fields, a key to oil migration. *Bulletin of the American Association of Petroleum Geologists*, **65**, 74–85.

Eckert A, Connolly PT (2007) Stress and fluid-flow interaction for the Coso Geothermal Field derived from 3D numerical models. *GRC Transactions*, **31**, 385–90.

Eckert A, Connolly P, Liu X (2014) Large-scale mechanical buckle fold development and the initiation of tensile fractures. *Geochemistry, Geophysics, Geosystems*, **15**, 4570–87.

Eckert A, Liu X (2014) An improved method for numerically modeling the minimum horizontal stress magnitude in extensional stress regimes. *International Journal of Rock Mechanics and Mining Sciences*, **70**, 581–92.

Evans MA, Fischer MP (2012) On the distribution of fluids in folds: A review of controlling factors and processes. *Journal of Structural Geology*, **44**, 2–24.

Frehner M (2011) The neutral lines in buckle folds. *Journal of Structural Geology*, **33**, 1501–8.

Garven G (1995) Continental scale groundwater flow and geologic processes. *Annual Review of Earth & Planetary Science*, **23**, 89–117.
Ge S, Garven G (1992) Hydromechanical modeling of tectonically driven groundwater flow with application to the Arkoma Foreland Basin. *Journal of Geophysical Research*, **97**, 9119–44.
Hubbert MK (1953) Entrapment of petroleum under hydrodynamic conditions. *Bulletin of the American Association of Petroleum Geologists*, **37**, 1954–2026.
Hubbert MK, Rubey WW (1959) Role of fluid pressure in mechanics of overthrust faulting I. Mechanics of fluid-filled porous solids and its application to overthrust faulting. *Geological Society of America Bulletin*, **70**, 115–66.
Hudleston PJ, Treagus SH (2010) Information from folds: a review. *Journal of Structural Geology*, **32**, 2042–71.
Ingebritsen SE, Manning CE (2010) Permeability of the continental crust: dynamic variations inferred from seismicity and metamorphism. *Geofluids*, **10**, 193–205.
Jaeger JC, Cook NG, Zimmerman R (2007) *Fundamentals of Rock Mechanics*. Blackwell Publishing Ltd, Oxford, UK.
Ju M, Yang J, Dai T (2009) Numerical simulation of tectonic deformation-driven fluid flow: Implications for ore genesis in the Dachang district, Guangxi. *China. Journal of Geochemical Exploration*, **101**, 53.
Mancktelow NS (1999) Finite-element modeling of single-layer folding in elasto-viscous materials: the effect of initial perturbation geometry. *Journal of Structural Geology*, **21**, 161–77.
Mancktelow NS (2008) Tectonic pressure: Theoretical concepts and modelled examples. *Lithos*, **103**, 149–77.
McLellan JG, Oliver NHS, Schaubs PM (2004) Fluid flow in extensional environments; numerical modelling with an application to Hamersley iron ores. *Journal of Structural Geology*, **26**, 1157–71.
Medina CR, Rupp JA, Barnes DA (2011) Effects of reduction in porosity and permeability with depth on storage capacity and injectivity in deep saline aquifers: A case study from the Mount Simon Sandstone aquifer. *International Journal of Greenhouse Gas Control*, **5**, 146–56.
Minkoff SE, Stone CM, Bryant S, Peszynska M, Wheeler MF (2003) Coupled fluid flow and geomechanical deformation. *Journal of Petroleum Science and Engineering*, **38**, 37–56.
Nakajima J, Tsuji Y, Hasegawa A (2009) Seismic evidence for thermally-controlled dehydration reaction in subducting oceanic crust. *Geophysical Research Letters*, **36**, L03303.
Nemcok M, Schamel S, Gayer R (2005) *Thrustbelts: Structural Architecture*, pp. 221–50. Thermal Regimes and Petroleum Systems. Cambridge University Press, Cambridge, UK.
Oliver J (1986) Fluids expelled tectonically from orogenic belts: their role in hydrocarbon migration and other geologic phenomena. *Geology*, **14**, 99–102.
Ord A, Oliver HS (1997) Mechanical controls on fluid flow during regional metamorphism: some numerical models. *Journal of Metamorphic Geology*, **15**, 345–59.
Ord A, Hobbs BE, Zhang Y, Broadbent GC, Brown M, Willetts G, Sorjonen-Ward P, Walshe JL, Zhao C (2002) Geodynamic modeling of the Century deposit, Mt Isa Province, Queensland. *Australian Journal of Earth Sciences*, **49**, 1011–39.
Price NJ (1966) *Fault and joint development in brittle and semi-brittle rock, Vol. 1*. Pergamon Press, Oxford, UK.
Price NJ, Cosgrove JW (1990) *Analysis of Geological Structures*. Cambridge University Press, Cambridge, UK.
Ramberg H (1963) Fluid dynamics of viscous buckling applicable to folding of layered rocks. *Bulletin of the American Association of Petroleum Geologists*, **47**, 484–505.
Ramsay JG (1967) *Folding and Fracturing of Rocks*. McGraw-Hill, New York, NY.
Schmalholz SM, Podladchikov Y (1999) Buckling versus folding: importance of viscoelasticity. *Geophysical Research Letters*, **26**, 2641–4.
Schmalholz SM, Podladchikov YY, Schmid DW (2001) A spectral/finite difference method for simulating large deformations of heterogeneous, viscoelastic materials. *Geophysical Journal International*, **145**, 199–208.
Sibson RH (1996) Structural permeability of fluid-driven fault-fracture meshes. *Journal of Structural Geology*, **18**, 1031–42.
Smart KJ, Ferrill DA, Morris AP (2009) Impact of interlayer slip on fracture prediction from geomechanical models of fault-related folds. *Bulletin of the American Association of Petroleum Geologists*, **93**, 1447–58.
Smith-Rouch LS (2006) Oligocene–Miocene maykop/diatom total petroleum system of the South Caspian Basin Province, Azerbaijan, Iran, and Turkmenistan. *U.S. Geological Survey Bulletin*, **2201-I**, 27.
Stephansson O (1974) Stress-induced diffusion during folding. *Tectonophysics*, **22**, 233–51.
Twiss RJ, Moores EM (2007) *Structural Geology*. 2nd edn. W.H. Freeman and Company, New York, NY.
Upton P (1998) Modeling localization of deformation and fluid flow in a compressional orogen: implications for the Southern Alps of New Zealand. *American Journal of Science*, **298**, 296–323.
Walder J, Nur A (1984) Porosity reduction and crustal pore pressure development. *Journal of Geophysical Research*, **89**(B13), 11539–48.
Yang J (2006) Finite element modeling of transient saline hydrothermal fluids in multi-faulted sedimentary basins: implications for ore-forming processes. *Canadian Journal of Earth Sciences*, **43**, 1331–40.
Zhang Y, Mancktelow NS, Hobbs BE, Ord A, Mühlhaus HB (2000) Numerical modelling of single-layer folding: clarification of an issue regarding the possible effect of computer codes and the influence of initial irregularities. *Journal of Structural Geology*, **22**, 1511–22.
Zhang Y, Lin G, Roberts P, Ord A (2007) Numerical modelling of deformation and fluid flow in the Shuikoushan district, Hunan Province, South China. *Ore Geology Reviews*, **31**, 261–78.
Zhang Y, Robinson J, Schaubs PM (2011) Numerical modelling of structural controls on fluid flow and mineralization. *Geoscience Frontiers*, **2**, 449–61.
Zhou Q, Birkholzer JT, Tsang CF, Rutqvist J (2008) A method for quick assessment of CO_2 storage capacity in closed and semi-closed saline formations. *International Journal of Greenhouse Gas Control*, **2**, 626–39.

APPENDIX

Scale evolution during single-layer buckling

As described in Section 'Numerical Modelling Approach', the initial depth of the folding layer is 1000 m and continuously increases with lateral shortening. In order to corre-

late the pore pressure distribution to the depth of the folding layer, the horizontal and vertical scales of the folding layer at various stages shortening are shown in Fig. A1. The influence of different permeabilities is negligible.

Fluid volume ratio

The total fluid volume, V_f, in the simulations is defined as:

$$V_f = s\phi V \quad (A1)$$

where s is the saturation, ϕ the porosity and V the bulk volume. The saturation is 100%. Thus, the fluid volume ratio, $n_f = V_f/V$, can be expressed as:

$$n_f = \phi \quad (A2)$$

Hence, the fluid volume ratio equals the porosity in this simulation. The initial porosity is changing with depth (after Medina *et al.* 2011) and the porosity decreases during buckling due to the increasing depth of overburden and lateral shortening. With an incompressible fluid and rock matrix, that is utilizing a Biot coefficient of $\alpha = 1$, the porosity reduction during shortening is expressed as:

$$\phi = \frac{\frac{E(1-\phi_0)}{3(1-2\nu)}\mathrm{In}\left(\frac{\sigma_0'^{iso}}{\sigma'^{iso}}\right) + \phi_0}{1 - \left(\frac{E(1-\phi_0)}{3(1-2\nu)}\mathrm{In}\left(\frac{\sigma_0'^{iso}}{\sigma'^{iso}}\right)\right)} \quad (A3)$$

where s is the Young's modulus, ν the Poisson ratio, ϕ_0 the initial porosity and σ'^{iso} the isotropic part of the effective stress tensor.

The fluid volume ratio, n_f, results for Model 1 ($k = 10^{-15}$ m^2) and Model 2 ($k = 10^{-23}$ m^2) at different stages of shortening are shown in Fig. A2. As described in Section 'Numerical Modelling Approach', the same initial porosity decrease with depth is assigned to the models and no difference is observed for the n_f distributions before buckling. For high-permeability models (i.e. Model 1), the fluid volume ratio distribution corresponds to the volumetric strain and a higher magnitude of n_f is found in regions of low volumetric strain. The results of n_f for the lowest permeability model ($k = 10^{-23}$ m^2) show that volumetric strain has reduced influence on the distribution of n_f, and no significant reduction of the magnitude of the fluid volume ratio is observed. This observation can be explained by this extreme low permeability, which results in limited fluid exchange between the folding layer and the matrix. The exchanged fluid volume (between folding layer and matrix) is 1% for Model 1 and 0.02% for Model 2 of its initial fluid volume after 50% shortening.

Evolution of pore pressure, fluid velocity and $\Delta P_p/\Delta t$ in Model 1

With a homogenous permeability no smaller than 10^{-17} m^2, hydrostatic pore pressure is achieved during shortening, and the pore pressure in the folding layer is continuously increasing due to the growing thickness of overburden. Due to the changing pore pressure during shortening, the fluid system is in a pseudo-hydrostatic state and the flow velocity represents the combination of reaching hydrostatic equilibrium and the influence of the volumetric strain distribution. To clarify the concept of pseudo-hydrostatic pore pressure, an additional step is added to Model 1. After 50% shortening, the lateral boundaries are constrained (i.e. zero strain rate is applied) and the state of deformation is conserved. Figure A3 shows the evolution of pore pressure, pore pressure increment rate ($\Delta P_p/\Delta t$) and fluid velocity in the limb of the folding layer of Model 1. It is observed that the pore pressure (red line in Fig. A3) increases with shortening with a constant vertical gradient (i.e. 9.81 MPa km^{-1}). However, the nature of the dynamic pore pressure evolution can be shown by the nonzero $\Delta P_p/\Delta t$ values throughout the deformation history resulting from the increasing overburden thickness. Figure A3 shows that the magnitudes of both $\Delta P_p/\Delta t$ and the fluid velocity increase with shortening until 50%, when shortening instantaneously stops and pore pressure becomes constant, that is $\Delta P_p/\Delta t = 0$. As a result, the fluid velocity decreases to zero. Thus, it can be concluded that the fluid velocity is partially influenced by the dynamic pore pressure evolution during shortening.

Material orientations

The proper orientation of the modelled material is crucial for the assigned anisotropic permeability. It is especially important for deformed rocks, where the enhanced horizontal permeability is expected to rotate during buckling and becomes parallel to the folding layer. In ABAQUS™, this can be achieved by specifying material orientations based on the local element coordinate orientations (Fig. A4). Before shortening, the material orientations are parallel to the global model coordinate system (Fig. A4A; i.e. parallel to the x-axis and z-axis in Fig. 1). During buckling, the material orientations rotate and remain either parallel or perpendicular to the fold (Fig. A4B,C). Thus, the enhanced horizontal permeability which is along the horizontal component of the material orientation remains parallel to the fold and thus helps to explain the layer parallel fluid flow observed in the modelling results.

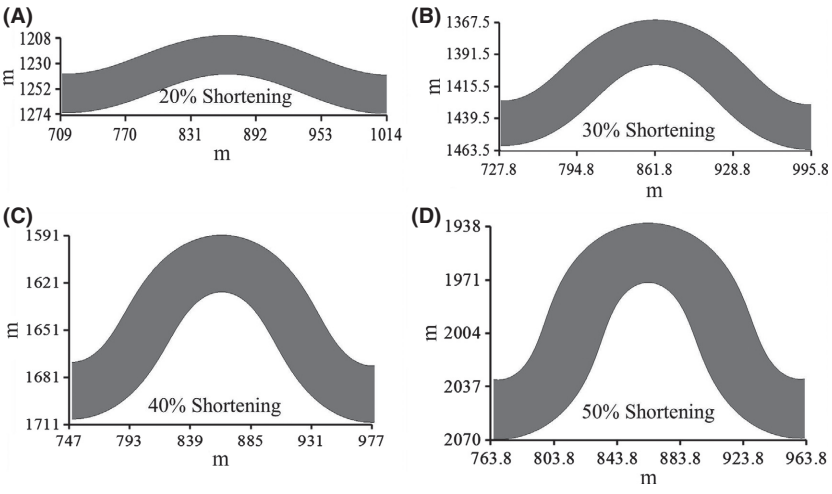

Fig. A1. Spatial references for each deformation stage of Model 1. (A) Fold geometry after 20% shortening. (B) Fold geometry after 30% shortening. (C) Fold geometry after 40% shortening. (D) Fold geometry after 50% shortening.

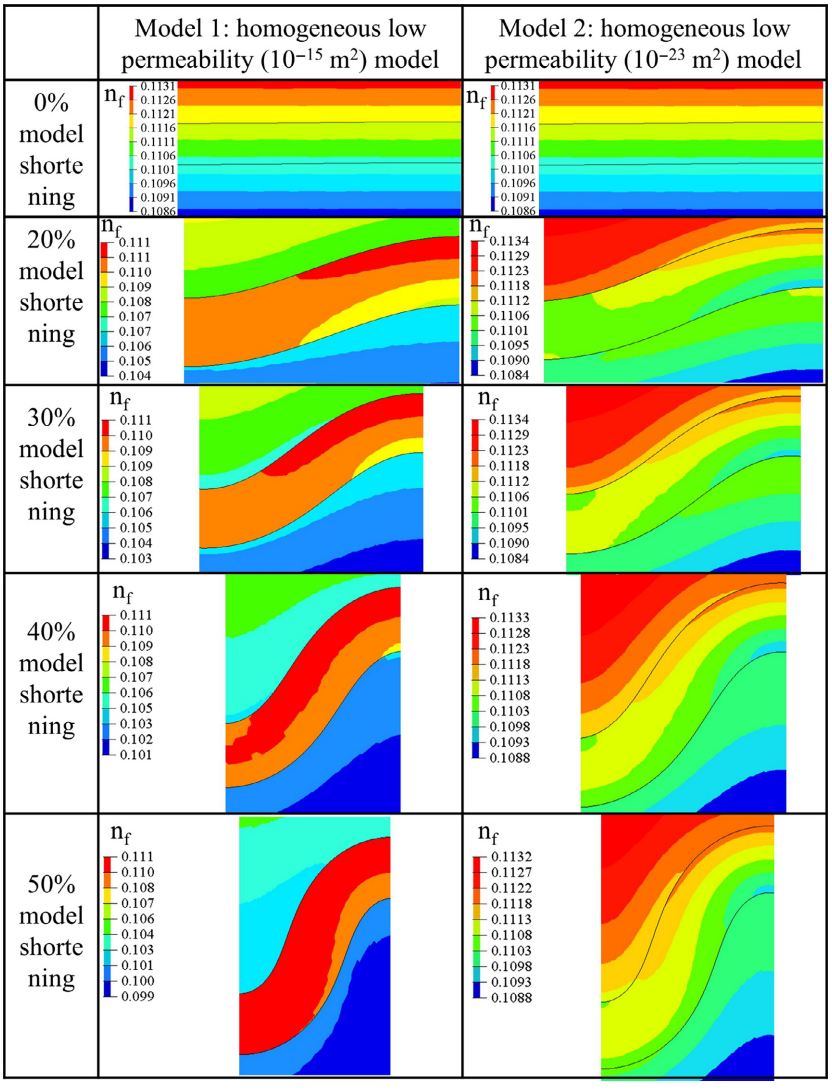

Fig. A2. Fluid volume ratio contours for Model 1 and Model 2 for 20, 30, 40 and 50% shortening.

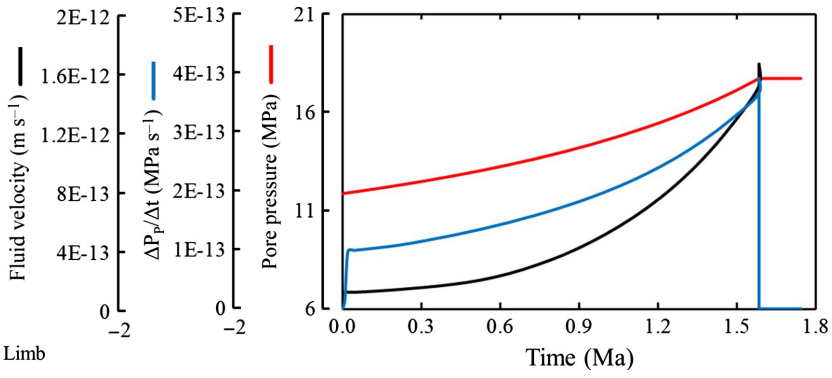

Fig. A3. Evolution of pore pressure, fluid velocity and $\Delta P_P/\Delta t$ at the fold limbs for Model 1 featuring a high permeability.

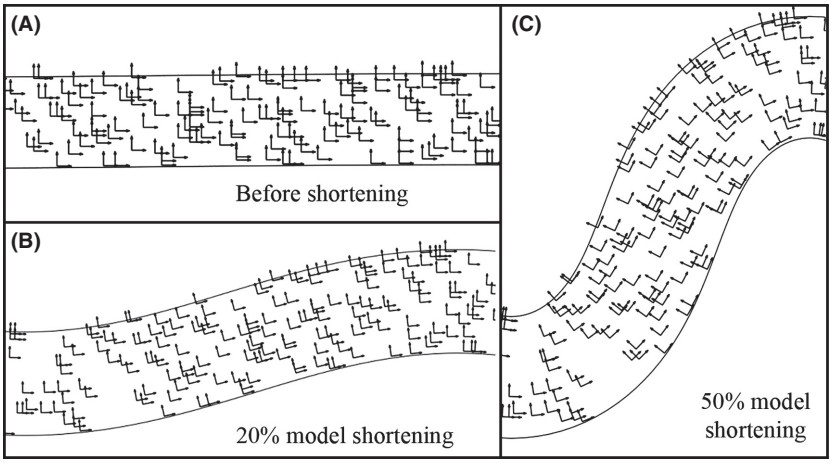

Fig. A4. Material orientations are specified such that the initial horizontal permeability remains layer parallel during buckling. (A) Material orientation before shortening. (B) Material orientation at 20% shortening. (C) Material orientation at 50% shortening.

GEOFLUIDS

Volume 16, Number 2, May 2016
ISSN 1468-8115

CONTENTS

WILEY
Blackwell

Geofluids* is abstracted/indexed in *Chemical Abstracts

This journal is available online at Wiley Online Library.
Visit onlinelibrary.wiley.com to search the articles and register for table of contents and e-mail alerts.